

# Reversible to Irreversible Transitions for ac Driven Skyrmions on Periodic Substrates

J. C. Bellizotti Souza<sup>1</sup>, N. P. Vizarim<sup>2</sup>, C. J. O. Reichhardt<sup>3</sup>, C. Reichhardt<sup>3</sup> and P. A. Venegas<sup>4</sup>

E-mail: [jc.souza@unesp.br](mailto:jc.souza@unesp.br)

<sup>1</sup> POSMAT - Programa de Pós-Graduação em Ciência e Tecnologia de Materiais, São Paulo State University (UNESP), School of Sciences, Bauru 17033-360, SP, Brazil

<sup>2</sup> Department of Electronics and Telecommunications Engineering, São Paulo State University (UNESP), School of Engineering, São João da Boa Vista 13876-750, SP, Brazil

<sup>3</sup> Theoretical Division and Center for Nonlinear Studies, Los Alamos National Laboratory, Los Alamos, New Mexico 87545, USA

<sup>4</sup> Department of Physics, São Paulo State University (UNESP), School of Sciences, Bauru 17033-360, SP, Brazil

## Abstract.

Using atomistic simulations, we investigate the dynamical behavior of magnetic skyrmions in dimer and trimer molecular crystal arrangements, as well as bipartite lattices at  $3/2$  and  $5/2$  fillings, under ac driving over a square array of anisotropy defects. For low ac amplitudes, at all fillings we find reversible motion where the skyrmions return to their original positions at the end of each ac drive cycle and the diffusion is zero. We also identify two distinct irreversible regimes. The first is a translating regime in which the skyrmions form channels of flow in opposing directions and translate by one substrate lattice constant per ac drive cycle. The translating state appears in the dimer and trimer states, and produces pronounced peaks in the diffusivity in the direction perpendicular to the external drive. For larger ac amplitudes, we find chaotic irreversible motion in which the skyrmions can randomly exchange places with each other over time, producing long-time diffusive behavior both parallel and perpendicular to the ac driving direction.

## 1. Introduction

A large variety of dynamic phenomena can emerge for many body systems under dc driving over random or periodic substrates [1]. Examples of such systems include colloidal particles [2, 3], type-II superconducting vortices [4, 5], active matter [6], sliding friction [7], and geological systems [8]. The flows may be strongly disordered or chaotic in the plastic flow regimes but ordered in elastic flow regimes [1]. If ac rather than dc driving is applied, even in the absence of a substrate it is possible for many body systems to undergo a transition from reversible behavior, where the particles return to the same positions after each ac drive cycle, to irreversible behavior, where the particles never return to their original positions. The irreversible flows can produce long time diffusive behavior even in the absence of thermal fluctuations. The transition from reversible to irreversible behavior was first studied in detail for periodically sheared colloidal particles [9], where the net displacement of the particles was measured after each shear cycle. In the reversible regime, the colloids returned to their initial configuration at the end of each cycle. In the irreversible regime, the configuration of the colloids changed from one cycle to the next, with the colloids exhibiting chaotic dynamics and undergoing long-term diffusive behavior after many cycles. Pine *et al.* [9] found that for fixed colloidal density, there was a critical ac drive amplitude above which irreversible behavior appeared, while if the ac amplitude was fixed, there was a critical density above which the motion became irreversible.

In further investigations of the periodically sheared colloidal system, Corte *et al.* [10] found that while the initial motion is always irreversible, the particles eventually organize into a steady state that may be either reversible or irreversible, depending on the distance traveled during the shearing process. Notably, the number of cycles required to reach this steady state diverges as a power law at a critical point, indicating that the reversible-irreversible transition is a nonequilibrium phase transition. In the colloidal system, the behavior becomes reversible when the particles are able to organize into a state where particle-particle collisions never occur. Additional investigations of reversible to irreversible (R-IR) transitions have since been performed in other systems with much stronger particle-particle interactions, where interactions between the particles remain important even in the reversible state. These include granular matter [11, 12], dislocations [13, 14], amorphous solids [15, 16, 17, 18], polycrystalline solids [19], type-II superconducting vortices [20, 21, 22] and, more recently, magnetic skyrmions [23].

Previous work on R-IR transitions for superconducting vortices and magnetic skyrmions was performed under coupling to a randomly disordered substrate. Far less is known about the nature of R-IR transitions for systems on periodic substrates [24], where commensuration effects can arise when the ratio of the number of particles to the number of substrate minima is an integer or a rational fraction [25, 26, 27, 1]. For commensurate conditions, the system generally adopts an ordered structure. This implies that under periodic shearing, different effects could arise compared to what is found for systems with random disorder. In this work we study R-IR transitions for magnetic skyrmions subjected to ac driving over periodic substrates for integer and rational fillings. Compared to the previous work on R-IR transitions in skyrmion systems [23], the two key differences in the present work are that we consider a periodic substrate, and that instead of using a point particle or Thiele equation approach where the skyrmions have no internal degrees of freedom, we perform atomistic simulations that permit the skyrmions to change both shape and size.

Magnetic skyrmions are particle-like topologically protected magnetic textures [28, 29] that exhibit many similarities to overdamped particles. Both minimize their repulsive interactions by forming a triangular array, can be set in motion by the application of external driving, and can

interact with material defects in several distinct ways [30, 1, 31]. The key difference between skyrmions and other overdamped particles is the presence of a non-dissipative Magnus force that causes the skyrmions, in clean samples, to move at an angle known as the intrinsic skyrmion Hall angle,  $\theta_{\text{sk}}^{\text{int}}$ , with respect to the external driving force [28, 32, 33, 34, 35, 36]. This Magnus force produces richer dynamical behavior, with a greater number of possible dynamical phases, for the skyrmions compared to other overdamped particles, since the skyrmion motion is not along the drive direction, but follows a finite angle. The Magnus force can also significantly change the interaction of the skyrmions with a substrate. In the limit of large Magnus forces, the skyrmion moves parallel rather than perpendicular to equipotential lines of the substrate potential [37]. For more moderate Magnus forces, the skyrmion picks up a velocity component that is perpendicular to the substrate force [31]. The rich dynamical behavior of skyrmions interacting with substrates has been intensively investigated in recent years, spanning topics that include periodic pinning [38, 39, 37, 40, 41, 42], interface guided motion [43, 44], ratchet effects [45, 46, 47, 48, 49], temperature and magnetic field gradients [50, 51, 52, 53], granular films [54, 55], parametric pumping [56], voltage-controlled perpendicular magnetic anisotropy (PMA) [57, 58], skyrmion lattice compression [59, 60], soliton motion along skyrmion chains [61, 62], pulse current modulation [63], strain driven motion [64], and motion through interaction with domain walls [65]. Skyrmions are bubble-like objects that can change shape and size, but most previous studies of R-IR transitions have focused on particles that have a fixed size and shape.

Recently, Souza *et al.* [66] reported the stabilization of skyrmion molecular crystals on triangular substrates. The skyrmion molecular crystals exhibited the same ordering as other molecular crystals found for superconducting vortices [67, 68, 69], colloidal particles [70, 71, 72, 73, 74], and Wigner crystals [75, 76]. These arrangements of particles are known as “molecular crystals” because, at integer fillings, particles trapped in individual substrate minima organize into dimer, trimer, and higher-order  $n$ -mer states that can exhibit an overall orientational order [69]. The dynamics of the particles in these dimer, trimer, or  $n$ -mer states could lead to novel behavior at R-IR transitions.

Using atomistic simulations, we simulate the dynamical behavior of different skyrmion molecular crystal arrangements, including dimers, trimers, and bipartite lattices with  $3/2$  and  $5/2$  fillings, under ac driving over a square array of sites with modified anisotropy. We measure the positions of the skyrmions after each ac drive cycle. In the irreversible regimes, the skyrmions change positions so that there is a finite long-time diffusivity, while in the reversible state, the diffusion is zero. At low ac amplitudes, we observe reversible skyrmion motion for all skyrmion arrangements, but we find that the ac amplitude range over which the motion remains reversible changes depending on the filling fraction. For higher ac amplitudes, we find peaks in the  $y$ -direction diffusivity, perpendicular to the driving direction, only for dimer and trimer fillings. At these peaks, the motion is irreversible since the diffusion is nonzero, and a portion of the skyrmions translate by a fixed upward or downward amount during each ac drive cycle in the form of an edge current. Even though the motion is irreversible, the trajectories are ordered. In this case, there is no net directed motion of skyrmions since half of the mobile skyrmions are moving in the  $+y$  direction and the other half are moving in the  $-y$  direction, so the system is not a ratchet. We also find that by using other fillings or applying even larger ac drive amplitudes, the skyrmions undergo chaotic irreversible motion with a finite diffusivity that is much lower than the diffusivity in the irreversible states with directed motion.

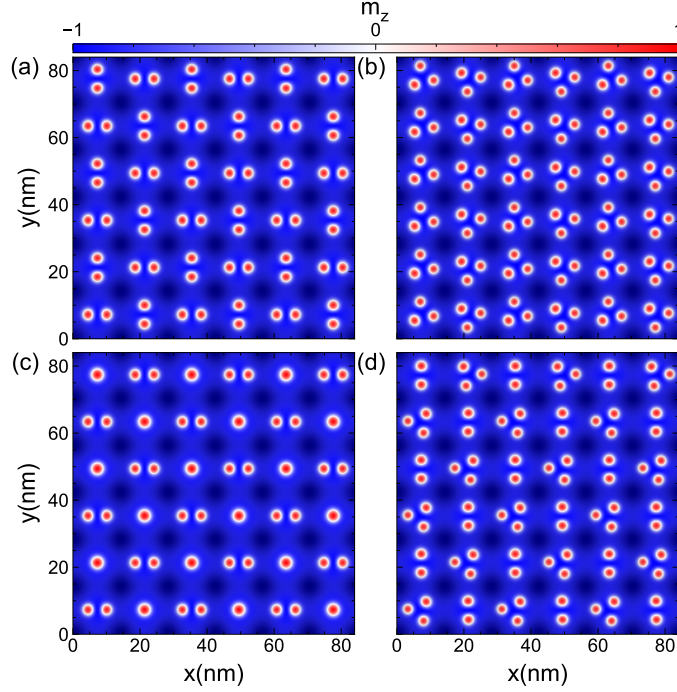


**Figure 1.** Images of the different initial skyrmion lattice arrangements used in this work. The PMA is plotted as a transparency overlay, with dark regions indicating high PMA. (a) Dimers forming an alternating pattern, or antiferromagnetic pattern, at  $N_{\text{sk}}/N_m = 2$  (b) Trimers in an alternating column pattern at  $N_{\text{sk}}/N_m = 3$ . (c) Bipartite lattice containing monomers and dimers at  $N_{\text{sk}}/N_m = 3/2$ . (d) Bipartite lattice containing dimers and trimers at  $N_{\text{sk}}/N_m = 5/2$ .

## 2. Methods

We employ atomistic simulations, which track the motion of individual atomic magnetic moments [77], to model Néel skyrmions in an ultrathin ferromagnetic sample. The sample is of size  $84 \text{ nm} \times 84 \text{ nm}$  and has periodic boundary conditions along the  $x$  and  $y$  directions. The sample anisotropy is given by  $K(x, y) = \frac{K_0}{4} \left[ \cos\left(\frac{2\pi x}{a_0}\right) + \cos\left(\frac{2\pi y}{a_0}\right) + 2 \right]$ , where  $K_0$  is the anisotropy depth,  $a_0 = 14 \text{ nm}$  is the substrate lattice constant, and there are  $N_m = 36$  minima of the anisotropy. This produces a substrate consisting of a periodic square array of defects. We apply a magnetic field perpendicular to the sample along  $-z$  at zero temperature  $T = 0 \text{ K}$ .

The Hamiltonian governing the atomistic dynamics is given by [77, 33, 78]:

$$\begin{aligned} \mathcal{H} = & - \sum_{i,j \in N} J_{ij} \mathbf{m}_i \cdot \mathbf{m}_j - \sum_{i,j \in N} \mathbf{D}_{ij} \cdot (\mathbf{m}_i \times \mathbf{m}_j) \\ & - \sum_i \mu \mathbf{H} \cdot \mathbf{m}_i - \sum_i K(x_i, y_i) (\mathbf{m}_i \cdot \hat{\mathbf{z}})^2 . \end{aligned} \quad (1)$$

The underlying lattice is a square arrangement of magnetic moments with lattice constant

$a = 0.5$  nm. The first term on the right hand side is the exchange interaction between the nearest neighbors contained in the set  $N$ , with an exchange constant of  $J_{ij} = J$  between magnetic moments  $i$  and  $j$ . The second term is the interfacial Dzyaloshinskii–Moriya interaction, where  $\mathbf{D}_{ij} = D\hat{\mathbf{z}} \times \hat{\mathbf{r}}_{ij}$  is the Dzyaloshinskii–Moriya vector between magnetic moments  $i$  and  $j$  and  $\hat{\mathbf{r}}_{ij}$  is the unit distance vector between sites  $i$  and  $j$ . The third term is the Zeeman interaction with an applied external magnetic field  $\mathbf{H}$ . Here  $\mu = \hbar\gamma$  is the magnitude of the magnetic moment and  $\gamma = 1.76 \times 10^{11}$  T<sup>-1</sup> s<sup>-1</sup> is the electron gyromagnetic ratio. The last term represents the perpendicular magnetic anisotropy (PMA) of the sample, where  $x_i$  and  $y_i$  are the spatial coordinates of the  $i$ th magnetic moment. Since we are considering ultrathin films, long-range dipolar interactions are small enough that they can be neglected [79].

The time evolution for the individual atomic magnetic moments is obtained using the LLG equation [80, 81]:

$$\frac{\partial \mathbf{m}_i}{\partial t} = -\gamma \mathbf{m}_i \times \mathbf{H}_i^{\text{eff}} + \alpha \mathbf{m}_i \times \frac{\partial \mathbf{m}_i}{\partial t} + \frac{pa^3}{2e} (\mathbf{j} \cdot \nabla) \mathbf{m}_i. \quad (2)$$

Here  $\gamma$  is the electron gyromagnetic ratio,  $\mathbf{H}_i^{\text{eff}} = -\frac{1}{\hbar\gamma} \frac{\partial \mathcal{H}}{\partial \mathbf{m}_i}$  is the effective magnetic field including all interactions from the Hamiltonian,  $\alpha$  is the phenomenological damping introduced by Gilbert, and the last term is the adiabatic spin-transfer-torque (STT), where  $p$  is the spin polarization,  $e$  the electron charge, and  $\mathbf{j}$  the applied current density. Use of this STT expression implies that the conduction electron spins are always parallel to the magnetic moments  $\mathbf{m}$ [33, 82]. The non-adiabatic terms can be neglected in this case, since they do not affect the skyrmion dynamics significantly under small driving forces [32]. The current density  $\mathbf{j}$  used in this work has the form  $\mathbf{j} = j \cos(2\pi ft) \hat{\mathbf{x}}$ , where  $j$  is the ac amplitude,  $f$  is the ac frequency, and  $t$  is the time.

We fix the following values in our simulations:  $\mu\mathbf{H} = 0.6(D^2/J)(-\hat{\mathbf{z}})$ ,  $\alpha = 0.3$ ,  $p = -1.0$ , and  $f = 0.1$  GHz. The material parameters are  $J = 1$  meV,  $D = 0.5J$ , and  $K_0 = 0.1J$ . For each simulation, the system is initialized in one of the configurations illustrated in Fig. 1. The numerical integration of Eq. 2 is performed using a fourth order Runge-Kutta method over 200 ns.

We measure the mean square displacement  $R_\alpha$  in each direction,  $\alpha = x, y$ :

$$R_\alpha(n) = \frac{1}{N_{\text{sk}}} \sum_i^{N_{\text{sk}}} [(\mathbf{r}_i(t_0 + nT) - \mathbf{r}_i(t_0)) \cdot \hat{\boldsymbol{\alpha}}]^2 \quad (3)$$

where  $N_{\text{sk}}$  is the number of skyrmions in the sample,  $n$  is the number of ac drive cycles that have elapsed,  $T = 1/f = 10$  ns is the ac drive period, and  $\mathbf{r}_i$  is the position of skyrmion  $i$ . From  $R_\alpha$ , we compute the effective diffusivity according to  $D_\alpha = R_\alpha/2t$ , following the same procedure used in Refs. [20, 9].

### 3. Effective Diffusivity

We first analyze how the effective diffusivity changes as the filling and ac amplitude  $j$  are changed. As shown in Fig. 2(a), for the dimer arrangement at  $N_{\text{sk}}/N_m = 2$ , we obtain  $D_x = 0$  and  $D_y = 0$  for ac amplitudes  $j \leq 2.7 \times 10^{10}$  A m<sup>-2</sup>. The absence of diffusion indicates that this is a reversible regime in which the skyrmions move back and forth under the ac driving, but return to their original positions at the end of each driving cycle and experience no net motion. An animation of the motion of the skyrmions in this reversible regime appears in the Supplemental Material [83]. Over the interval  $2.8 \times 10^{10}$  A m<sup>-2</sup>  $\leq j \leq 3.0 \times 10^{10}$  A m<sup>-2</sup>, we find that  $D_y$  increases abruptly to  $D_y \geq 160$  nm<sup>2</sup> ns<sup>-1</sup> while  $D_x$  remains at  $D_x = 0$ , indicating a net displacement of individual

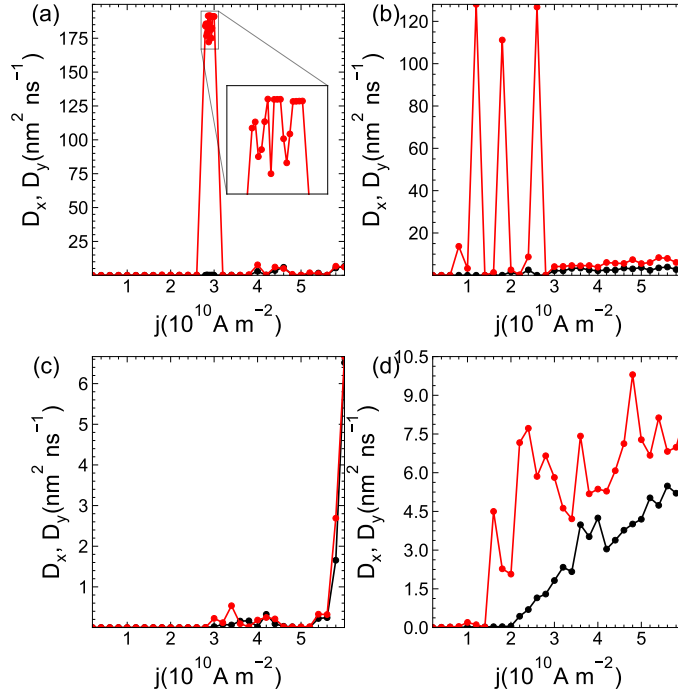


**Figure 2.** Diffusivities  $D_x$  (black) and  $D_y$  (red) vs ac amplitude  $j$  at different fillings. (a)  $N_{\text{sk}}/N_m = 2$ , the antiferromagnetic dimer arrangement from Fig. 1(a). Inset: a blowup of the region spanning  $2.7 \times 10^{10} \text{ A m}^{-2} \leq j \leq 3.1 \times 10^{10} \text{ A m}^{-2}$ . (b)  $N_{\text{sk}}/N_m = 3$ , the alternating column trimer arrangement from Fig. 1(b). (c)  $N_{\text{sk}}/N_m = 3/2$ , the bipartite monomer and dimer lattice from Fig. 1(c). (d)  $N_{\text{sk}}/N_m = 5/2$ , the bipartite dimer and trimer lattice from Fig. 1(d). Strong peaks in  $D_y$  appear in panels (a) and (b) for the dimer and trimer states, but are absent for both of the bipartite lattices.

skyrmions only along the  $y$  direction. When  $j$  is increased further,  $D_y$  drops abruptly back to  $D_y = 0$ . For  $j > 3 \times 10^{10} \text{ A m}^{-2}$ ,  $D_x$  and  $D_y$  are very small compared to the peak values of  $D_y$ ; however, they are not equal to zero, indicating that the skyrmions are in an irreversible state with finite net motion of the skyrmions from cycle to cycle.

We find very different behavior for the  $N_{\text{sk}}/N_m = 3$  trimer state, as shown in Fig. 2(b). Under very low ac amplitudes,  $j \leq 0.8 \times 10^{10} \text{ A m}^{-2}$ ,  $D_x = D_y = 0$ . These low ac amplitudes are not strong enough to dislodge individual skyrmions from the potential minimum in which they are trapped, producing an oscillation inside the potential minimum with no net translation. A small peak in  $D_y$  appears for  $j = 0.8 \times 10^{10} \text{ A m}^{-2}$ , indicating a net motion of the skyrmions along the  $y$  direction. After this first small peak at  $j = 0.8 \times 10^{10} \text{ A m}^{-2}$ , there are three larger peaks in  $D_y$  at  $j = 1.2 \times 10^{10} \text{ A m}^{-2}$ ,  $j = 1.8 \times 10^{10} \text{ A m}^{-2}$ , and  $j = 2.6 \times 10^{10} \text{ A m}^{-2}$ , with  $D_y$  returning to  $D_y = 0$  between each peak and  $D_x$  remaining at  $D_x = 0$  throughout the entire current interval. As was the case for the dimer filling, the peaks in  $D_y$  indicate that there is a net displacement of the skyrmions along the  $y$  direction only. These peaks have different  $D_y$  values, indicating that different types of motion occur for each peak. The same is true for the different peak  $D_y$  values in Fig. 2(a). For higher ac amplitudes of  $j \geq 3 \times 10^{10} \text{ A m}^{-2}$ , both  $D_x$  and  $D_y$  have nonzero values,

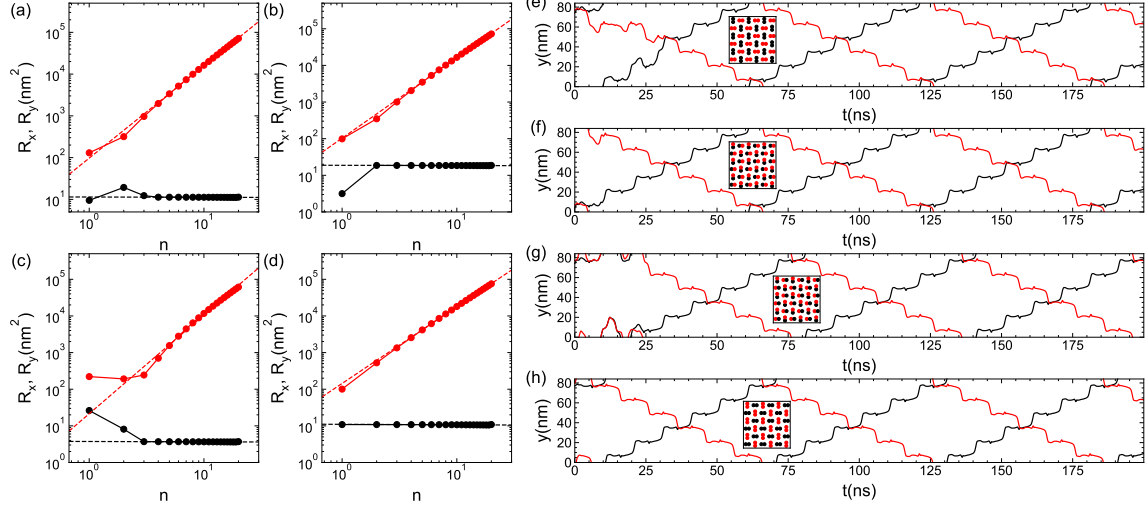


**Figure 3.** (a-d)  $R_x$  (black) and  $R_y$  (red) vs ac drive cycle number  $n$  for the  $N_{sk}/N_m = 2$  dimer arrangement from Fig. 1(a) at ac drive amplitudes of (a)  $j = 2.8 \times 10^{10} \text{ A m}^{-2}$ , (b)  $j = 2.85 \times 10^{10} \text{ A m}^{-2}$ , (c)  $j = 2.875 \times 10^{10} \text{ A m}^{-2}$ , and (d)  $j = 3 \times 10^{10} \text{ A m}^{-2}$ . Dashed lines are the fitted curves used to compute  $D_x$  and  $D_y$ . (e-h) The  $y$  position of two selected skyrmions versus time in samples with (e)  $j = 2.8 \times 10^{10} \text{ A m}^{-2}$ , (f)  $j = 2.85 \times 10^{10} \text{ A m}^{-2}$ , (g)  $j = 2.875 \times 10^{10} \text{ A m}^{-2}$ , and (h)  $j = 3 \times 10^{10} \text{ A m}^{-2}$ . The curves are colored according to the net motion of each skyrmion:  $+y$  (black) or  $-y$  (red). When the skyrmion crosses the periodic boundary, the curve jumps from the top to the bottom of the panel or vice versa. The insets show the dimer arrangement colored according to the net motion of each skyrmion,  $+y$  (black) or  $-y$  (red). In panel (e), all vertically oriented dimers have a net  $+y$  motion and all horizontally oriented dimers have a net  $-y$  motion. In panel (f), the upper skyrmion of each vertically oriented dimer moves along  $-y$  and the lower skyrmion moves along  $+y$ , while the left skyrmion of each horizontally oriented dimer moves along  $-y$  and the right skyrmion moves along  $+y$ . In panel (g), the motion is as in panel (f) except that the left skyrmion of each horizontally oriented dimer moves along  $+y$  and the right skyrmion moves along  $-y$ . In panel (h) all vertically oriented dimers have a net  $-y$  motion and all horizontally oriented dimers have a net  $+y$  motion. An animation showing the skyrmions motion from panels (h) appears in the Supplemental Material [83].

indicating a chaotic irreversible motion of the skyrmions.

For the bipartite monomer and dimer lattice at  $N_{sk}/N_m = 3/2$ , Fig. 2(c) shows that the behavior of  $D_x$  and  $D_y$  is much simpler than for the dimer and trimer arrangements. There are no strong peaks in either  $D_x$  or  $D_y$ , and over most of the range of ac amplitudes considered here,  $j < 3 \times 10^{10} \text{ A m}^{-2}$ ,  $D_x = 0$  and  $D_y = 0$ , indicating that the motion is reversible. For higher ac amplitude values, the skyrmions begin to move in a chaotic irreversible fashion. The behavior of the bipartite dimer and trimer lattice at  $N_{sk}/N_m = 5/2$  in Fig. 2(d) is very similar, but has a reduced ac amplitude interval,  $j \leq 1.4 \times 10^{10} \text{ A m}^{-2}$ , of reversible motion. The values of  $D_x$  and  $D_y$  observed in Fig. 2(c, d) in the irreversible state are similar to the values of  $D_x$  and  $D_y$  found in Fig. 2(b) for chaotic irreversible motion at  $j \geq 3 \times 10^{10} \text{ A m}^{-2}$ .

#### 4. Dimer Peak Motion

We now focus on the dynamical behavior of the skyrmions at the dimer filling of  $N_{\text{sk}}/N_m = 2$  in irreversible states with  $D_y \neq 0$ . Figure 3(a-d) and Fig. 3(e-h) show the mean square displacement and individual  $y$  trajectories, respectively, for samples at ac amplitudes of  $j = 2.8 \times 10^{10} \text{ A m}^{-2}$ ,  $j = 2.85 \times 10^{10} \text{ A m}^{-2}$ ,  $j = 2.875 \times 10^{10} \text{ A m}^{-2}$ , and  $j = 3 \times 10^{10} \text{ A m}^{-2}$ , which fall within the region of large  $D_y$  values in Fig. 2(a). The lowest ac amplitude that produces irreversible behavior in Fig. 2(a) is  $j = 2.8 \times 10^{10} \text{ A m}^{-2}$ , and we present  $R_x$  and  $R_y$  versus ac drive cycle number  $n$  for this ac amplitude value in Fig. 3(a).  $R_y$  increases with  $n$  while  $R_x$  remains constant. Both  $R_x$  and  $R_y$  exhibit a transient behavior for  $n < 3$ , during which the skyrmions adjust themselves to the presence of the ac driving. This transient motion is also visible at small times  $t < 20 \text{ ns}$  in Fig. 3(e), where we plot the time dependence of the  $y$  position for two selected skyrmions. The colors of the curves, black for  $+y$  and red for  $-y$ , indicate the direction of net motion. The inset shows the dimer arrangement with skyrmions colored according to their net displacement. After the transient motion period, all skyrmions from the vertically oriented dimers move along  $+y$ , while all skyrmions from the horizontally oriented dimers move along  $-y$ . The  $+y$  and  $-y$  motions are out of phase by half of an ac driving period, since during the  $+x$  portion of the ac driving cycle, the skyrmions from the horizontally oriented dimers act as obstacles for the skyrmions from the vertically oriented dimers. These roles reverse during the  $-x$  portion of the ac driving cycle. All of the  $+y$  moving skyrmions are in phase with each other, and all of the  $-y$  moving skyrmions are in phase with each other.

For a larger ac drive amplitude of  $j = 2.85 \times 10^{10} \text{ A m}^{-2}$ , shown in Fig. 3(b, f), the dynamical behavior remains very similar, but the duration of the transient motion and the net direction of motion of individual skyrmions changes. Figure 3(b) indicates that the transient motion appears only for  $n < 2$ , corresponding to 10 ns as shown in Fig. 3(f). As was the case at the lower value of  $j$  above, half of the skyrmions have a net  $+y$  displacement and the other half have a net  $-y$  displacement, but the spatial distribution of these displacements is different. For each vertically oriented dimer, the upper skyrmion moves in the  $-y$  direction and the lower skyrmion moves in the  $+y$  direction. For each horizontally oriented dimer, the left skyrmion moves in the  $+y$  direction and the right skyrmion moves in the  $-y$  direction.

Further increasing the ac amplitude to  $j = 2.875 \times 10^{10} \text{ A m}^{-2}$ , has little impact on the dynamical behavior, as shown in Fig. 3(c, g). Now the transient motion extends over the time period  $n < 3$ , as shown in Fig. 3(c), which corresponds to 20 ns in Fig. 3(g). There is a subtle change in the spatial distribution of the skyrmion motion compared to Fig. 3(b, f). For the horizontally oriented dimers, the left skyrmion now moves in the  $-y$  direction instead of the  $+y$  direction, and the right skyrmion moves in the  $+y$  direction instead of the  $-y$  direction. This subtle change is responsible for the increase in the duration of the transient motion.

At an ac amplitude of  $j = 3 \times 10^{10} \text{ A m}^{-2}$ , illustrated in Fig. 3(d, h), the dynamical behavior changes again. The transient time is almost zero, meaning that skyrmions start to move with their steady state net  $y$  displacement after the first ac cycle. The spatial distribution of skyrmion motion is also different. All vertically oriented dimers have a net  $-y$  displacement while all horizontally oriented dimers have a net  $+y$  displacement. This is opposite from the motion found in Fig. 3(e) at  $j = 2.8 \times 10^{10} \text{ A m}^{-2}$ .

For each of the four values of  $j$  described above, all of the skyrmions that are moving along  $+y$  travel in phase with each other, and all of the skyrmions that are moving along  $-y$  travel in phase with each other. Additionally, the  $+y$  and  $-y$  motions have the same average



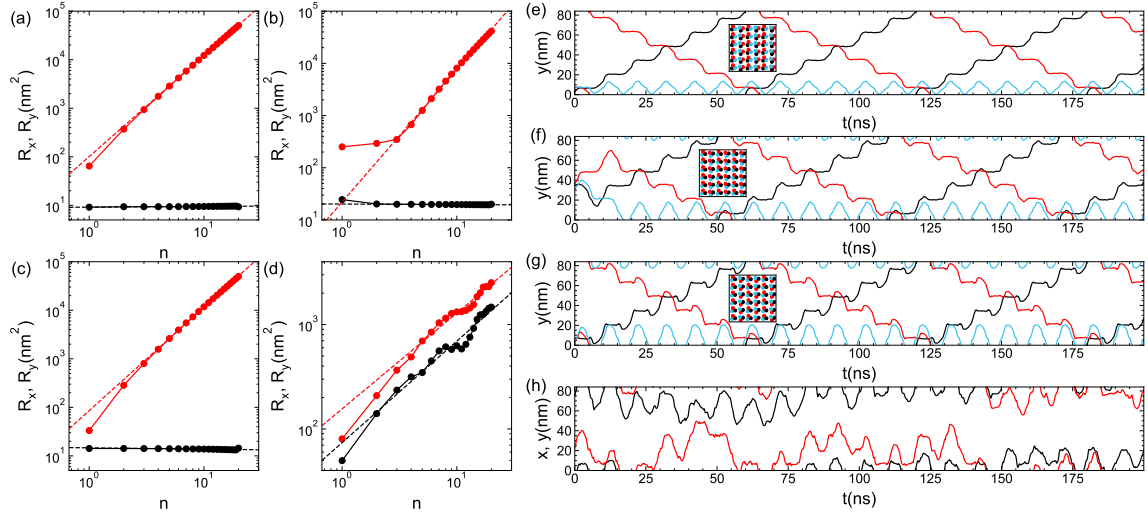


**Figure 4.** (a-d)  $R_x$  (black) and  $R_y$  (red) vs ac drive cycle number  $n$  for the  $N_{\text{sk}}/N_m = 3$  trimer arrangement from Fig. 1(b) at ac drive amplitudes of (a)  $j = 1.2 \times 10^{10} \text{ A m}^{-2}$ , (b)  $j = 1.8 \times 10^{10} \text{ A m}^{-2}$ , (c)  $j = 2.6 \times 10^{10} \text{ A m}^{-2}$ , and (d)  $j = 6 \times 10^{10} \text{ A m}^{-2}$ . Dashed lines are the fitted curves used to compute  $D_x$  and  $D_y$ . (e-g) The  $y$  position of three selected skyrmions versus time in samples with (e)  $j = 1.2 \times 10^{10} \text{ A m}^{-2}$ , (f)  $j = 1.8 \times 10^{10} \text{ A m}^{-2}$ , and (g)  $j = 2.6 \times 10^{10} \text{ A m}^{-2}$ . The curves are colored according to the net motion of each skyrmion:  $+y$  (black),  $-y$  (red), and oscillating with no net motion (blue). When the skyrmion crosses the periodic boundary, the curve jumps from the top to the bottom of the panel or vice versa. Insets show the spatial distribution of the direction of skyrmion motion. (h)  $x$  (black) and  $y$  (red) position of a selected skyrmion versus time for a chaotic irreversible system at  $j = 6 \times 10^{10} \text{ A m}^{-2}$ . An animation of the skyrmions motion from panel(e) appears in the Supplemental Material [83].

velocity of  $|\langle v_y \rangle| = 1.4 \text{ m/s}$ , which is equal to translation by one substrate lattice constant per ac cycle,  $|\langle v_y \rangle| = a_0/T$ . There is, however, no net dc motion in the sample, since equal numbers of skyrmions translate along  $+y$  and  $-y$ . An animation showing the motion of the skyrmions at  $j = 3 \times 10^{10} \text{ A m}^{-2}$ , with the same coloring conventions from Fig. 3(e-h), appears in the Supplemental Material [83].

## 5. Trimer Peak Motion

We now analyze the sharp  $D_y$  peaks present in Fig. 2(b) for the  $N_{\text{sk}}/N_m = 3$  trimer skyrmion arrangement. We do not specifically treat the small peak at  $j = 0.8 \times 10^{10} \text{ A m}^{-2}$ , since its value is comparable to the value found for chaotic motion at larger  $j$  and the system exhibits no interesting ordered movement.

The first sharp  $D_y$  peak observed in Fig. 2(b) appears at  $j = 1.2 \times 10^{10} \text{ A m}^{-2}$ , where  $D_y \approx 130 \text{ nm}^2 \text{ ns}^{-1}$  and  $D_x = 0$ . The corresponding values of  $R_x$  and  $R_y$  are plotted in Fig. 4(a).  $R_x$  remains constant as  $n$  increases, but  $R_y$  increases with increasing  $n$ , indicating a net skyrmion displacement along the  $y$  direction only. In Fig. 4(e) we plot the  $y$  position as a function of time for three representative skyrmions, one moving along  $+y$ , one moving along  $-y$ , and one oscillating with no net motion. The oscillating skyrmions act as an intermediary to facilitate the  $+y$  and  $-y$

movement of the other skyrmions. Skyrmions moving along  $+y$  are out of phase by half an ac drive period from skyrmions moving along  $-y$ , while the oscillating skyrmions move in phase with the ac drive. All skyrmions moving in a particular direction are in phase with each other, meaning that the  $+y$  skyrmions are in phase with each other, the  $-y$  skyrmions are in phase with each other, and the oscillating skyrmions are in phase with each other. The transient motion at this ac amplitude is very brief and lasts only one ac drive cycle, as seen in Fig. 4(a). The inset of Fig. 4(e) indicates the spatial distribution of the skyrmion motion. In the odd (first, third, and fifth) columns of trimers, where the trimer tips are oriented upward, the topmost skyrmion moves along  $-y$ , the rightmost skyrmion oscillates, and the leftmost skyrmion moves along  $+y$ . In the even (second, fourth, and sixth) columns of trimers, where the trimer tips are oriented downward, the bottommost skyrmion moves along  $+y$ , the rightmost skyrmion moves along  $-y$ , and the leftmost skyrmion oscillates. Viewed clockwise from the  $-y$  skyrmion, the order of motion of the skyrmions in each trimer is  $-y$ , oscillate,  $+y$  for the odd columns and  $-y$ ,  $+y$ , oscillate for the even columns.

The second  $D_y$  peak occurs at  $j = 1.8 \times 10^{10} \text{ A m}^{-2}$ , and has a slightly reduced value of  $D_y \approx 110 \text{ nm}^2 \text{ ns}^{-1}$ . The plots of  $R_x$  and  $R_y$  for this current, shown in Fig. 4(b), have behavior very similar to that found for the first peak in  $D_y$ , with  $R_x$  remaining constant as a function of  $n$  and  $R_y$  increasing with increasing  $n$ . The transient motion lasts for nearly three ac drive cycles, corresponding to approximately 30 ns in Fig. 4(f). The dynamical behavior of the trimers is very similar what was shown in Fig. 4(e), with each skyrmion exhibiting either  $+y$ ,  $-y$ , or oscillatory motion depending on its position inside the trimer. The spatial distribution of this motion is modified at this higher value of  $j$ , as seen by comparing the insets of Fig. 4(e) and Fig. 4(f). In all columns, whether even or odd, the upper leftmost skyrmion moves along  $-y$ , the upper rightmost skyrmion moves along  $+y$ , and the lower leftmost skyrmion oscillates. Viewed clockwise from the  $-y$  skyrmion, the order of motion of the skyrmions in all trimers is  $-y$ ,  $+y$ , oscillate. The fact that the motion of all trimers synchronizes independent of whether the trimer is in an odd or even column could be the reason that the peak value of  $D_y$  is somewhat diminished and the transient time is extended.

The last  $D_y$  peak for the trimer arrangement falls at  $j = 2.6 \times 10^{10} \text{ A m}^{-2}$ , where we find  $D_y \approx 130 \text{ nm}^2 \text{ ns}^{-1}$ , a higher value than what appears for  $j = 1.8 \times 10^{10} \text{ A m}^{-2}$ . The corresponding  $R_x$  and  $R_y$  versus  $n$  curves plotted in Fig. 4(c) are very similar to those found for the other  $D_y$  peaks, with  $R_x$  remaining constant and  $R_y$  increasing with the number of ac drive cycles. The transient time at this ac amplitude is reduced compared to the transient time observed in Fig. 4(b), and lasts for only one ac drive cycle, corresponding to  $t < 10 \text{ ns}$  in Fig. 4(g). As with the other peaks in  $D_y$ , for the dynamical behavior of the skyrmions we find that each skyrmion either moves in the  $+y$  or  $-y$  direction or oscillates about a fixed point. The spatial distribution of the skyrmion motion, in the inset of Fig. 4(g), is different from that at the other peaks in  $D_y$ . Trimers in odd columns exhibit the same ordering found in Fig. 4(f), with the topmost skyrmion moving along  $-y$ , the lower rightmost skyrmion moving along  $+y$ , and the lower leftmost skyrmion oscillating. Trimers in even columns have an ordering different from that found for other values of  $j$ , with the bottommost skyrmion moving along  $-y$ , the upper leftmost skyrmion oscillating, and the upper rightmost skyrmion moving along  $+y$ . Viewed clockwise from the  $-y$  skyrmion, the order of motion of the skyrmions is  $-y$ ,  $+y$ , oscillate for the odd columns and  $-y$ , oscillate,  $+y$  for the even columns. In both Fig. 4(e) and Fig. 4(g), where the order of trimer motion reverses from one column to the next, the  $D_y$  peak values are higher compared to the case in Fig. 4(f) where all columns have the same order of trimer motion. The average skyrmion displacement velocities are, however, the same in all cases,  $|\langle v_y \rangle| = a_0/T$ , meaning that all skyrmions that undergo a net displacement translate

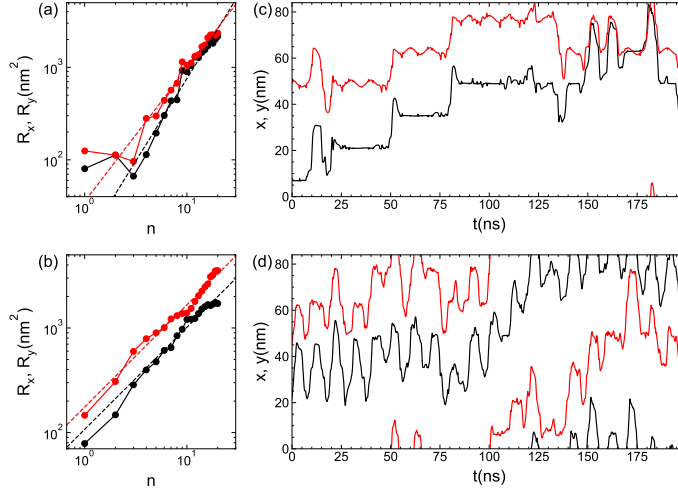


**Figure 5.** (a,b)  $R_x$  (black) and  $R_y$  (red) vs ac drive cycle number  $n$  at  $j = 6 \times 10^{10} \text{ A m}^{-2}$  for (a) the  $N_{sk}/N_m = 3/2$  bipartite monomer and dimer lattice and (b) the  $N_{sk}/N_m = 5/2$  bipartite dimer and trimer lattice. Dashed lines are the fitted curves used to compute  $D_x$  and  $D_y$ . (c,d)  $x$  (black) and  $y$  (red) position of a selected skyrmion versus time at  $j = 6 \times 10^{10} \text{ A m}^{-2}$  in (c) the  $N_{sk}/N_m = 3/2$  bipartite monomer and dimer lattice and (d) the  $N_{sk}/N_m = 5/2$  bipartite dimer and trimer lattice. Animations showing the skyrmion motion are available in the Supplemental Material [83].

by one substrate lattice constant per ac drive period. This is the same velocity observed for the dimer system.

Figure 4(d) shows the values of  $R_x$  and  $R_y$  versus  $n$  for the trimer system at  $j = 6 \times 10^{10} \text{ A m}^{-2}$ . At this ac amplitude the skyrmions do not exhibit an ordered motion, but instead undergo an irreversible chaotic motion. Both  $R_x$  and  $R_y$  increase with increasing  $n$ . This is very different from the behavior at peak values of  $D_y$ , where  $R_x$  remained constant while  $R_y$  increased with increasing  $n$ . The values of  $R_x$  and  $R_y$  for the disordered or chaotic irreversible motion are two orders of magnitude smaller than the value of  $R_y$  that appears for ordered irreversible motion. This reduction can be seen in Fig. 2(b), where for ac amplitudes  $j \geq 3 \times 10^{10} \text{ A m}^{-2}$ , the skyrmions exhibit an irreversible chaotic motion with finite  $D_x$  and  $D_y$  that have values much smaller than the peak values of  $D_y$  that appear for the ordered irreversible motion. The  $x$  and  $y$  positions of a representative skyrmion are plotted as a function of time at  $j = 6 \times 10^{10} \text{ A m}^{-2}$  in Fig. 4(h). The skyrmion motion is chaotic, and the displacement velocity is greatly reduced compared to the velocity that appears for the irreversible ordered motion. An animation of the motion of the trimers at  $j = 3 \times 10^{10} \text{ A m}^{-2}$  appears in the Supplemental Material [83].

## 6. Bipartite Lattices

Finally, we analyze the  $N_{sk}/N_m = 3/2$  bipartite monomer and dimer lattice and the  $N_{sk}/N_m = 5/2$  bipartite dimer and trimer lattice in Fig. 5. The low values of  $D_x$  and  $D_y$  in Fig. 2(c,d) for both bipartite lattices indicates that neither undergoes any type of ordered motion, but both show only chaotic irreversible motion. The  $N_{sk}/N_m = 3/2$  bipartite lattice first enters the chaotic motion

regime at large ac driving amplitudes, while the  $N_{\text{sk}}/N_m = 5/2$  bipartite lattice already exhibits chaotic motion under low ac drive amplitudes.

The  $R_x$  and  $R_y$  versus  $n$  curves for the  $N_{\text{sk}}/N_m = 3/2$  bipartite lattice in Fig. 5(a) both increase with increasing  $n$ . This is the expected behavior for chaotic motion, and matches what was observed in the trimer system under large ac drive amplitudes in Fig. 4(d). The values of  $R_x$  and  $R_y$  are two to three orders of magnitude smaller than the  $R_y$  values that appear during ordered motion, such as in Fig. 4(a-c). We illustrate the chaotic motion in Fig. 5(c) by plotting the  $x$  and  $y$  positions of a selected skyrmion as a function of time. The skyrmion motion has no well defined behavior, and the skyrmion diffuses through the sample over time. The same dynamical behavior is observed for the  $N_{\text{sk}}/N_m = 5/2$  bipartite lattice, as shown in Fig. 5(b), where both  $R_x$  and  $R_y$  increase with increasing  $n$ , but maintain values that are two to three orders of magnitude smaller than the values of  $R_y$  found for ordered motion. The  $x$  and  $y$  positions of a selected skyrmion versus time, plotted in Fig. 5(d), indicate the presence of chaotic motion. There is greater variability in the motion as a function of time compared to Fig. 5(c) due to the higher total filling fraction in the  $N_{\text{sk}}/N_m = 5/2$  bipartite lattice, which lowers the effective depinning threshold and enables the skyrmions to diffuse around the sample with higher mobility. Animations showing the chaotic skyrmion motion for the bipartite lattices at  $j = 6 \times 10^{10} \text{ A m}^{-2}$  are available in the Supplemental Material [83].

## 7. Summary

Using atomistic simulations, we investigated the reversible and irreversible behavior of ac driven skyrmions interacting with a periodic substrate for dimer, trimer, bipartite monomer and dimer, and bipartite dimer and trimer fillings. We find that under low ac amplitudes, all of the systems exhibit reversible dynamics in which all skyrmions in the sample return to their starting positions and the long time diffusion both parallel and perpendicular to the applied ac drive is zero. At larger ac amplitudes for the dimer and trimer systems, we observe pronounced peaks in the perpendicular diffusion  $D_y$  while the parallel diffusion  $D_x$  remains zero, indicating that individual skyrmions are undergoing one-dimensional directed motion along the  $y$  direction. In this ordered irreversible state, the skyrmions move one lattice constant per ac drive cycle in the translating regimes. For the dimers, half of the skyrmions move along  $+y$  and the other half move along  $-y$ , while for the trimers, a third of the skyrmions move along  $+y$ , a third move along  $-y$ , and the remaining third undergo confined oscillatory motion, so that there is no net skyrmion motion for either the dimer or trimer system. Under large ac drive amplitudes, we find irreversible chaotic motion of the dimers, trimers, and bipartite lattices. During the chaotic motion, the skyrmions diffuse throughout the sample in both the  $x$  and  $y$  directions. In the chaotic phases, the displacements grow diffusively, while in the translating phase, the displacements grow ballistically. Our results suggest a very precise way of controlling the skyrmion motion under ac driving for different skyrmion arrangements. The constant ballistic velocity of one substrate lattice constant per ac period can be exploited to construct spintronic devices in which the skyrmion motion and velocity must be carefully regulated.

## Acknowledgments

We gratefully acknowledge the support of the U.S. Department of Energy through the LANL/LDRD program for this work. This work was supported by the US Department of Energy through the Los Alamos National Laboratory. Los Alamos National Laboratory is operated by Triad National

Security, LLC, for the National Nuclear Security Administration of the U. S. Department of Energy (Contract No. 892333218NCA000001). J.C.B.S acknowledges funding from Fundação de Amparo à Pesquisa do Estado de São Paulo - FAPESP (Grant 2023/17545-1). We would like to thank Dr. Felipe F. Fanchini for providing the computational resources used in this work. These resources were funded by the Fundação de Amparo à Pesquisa do Estado de São Paulo - FAPESP (Grant: 2021/04655-8).

## References

- [1] C. Reichhardt and C. J. Olson Reichhardt. Depinning and nonequilibrium dynamic phases of particle assemblies driven over random and ordered substrates: a review. *Rep. Prog. Phys.*, 80(2):26501, 2017.
- [2] A. Pertsinidis and X. S. Ling. Statics and dynamics of 2D colloidal crystals in a random pinning potential. *Phys. Rev. Lett.*, 100(2):028303, 2008.
- [3] P. Tierno. Depinning and collective dynamics of magnetically driven colloidal monolayers. *Phys. Rev. Lett.*, 109(19):198304, 2012.
- [4] S. Bhattacharya and M. J. Higgins. Dynamics of a disordered flux line lattice. *Phys. Rev. Lett.*, 70(17):2617–2620, 1993.
- [5] G. Shaw, P. Mandal, S. S. Banerjee, A. Niazi, A. K. Rastogi, A. K. Sood, S. Ramakrishnan, and A. K. Grover. Critical behavior at depinning of driven disordered vortex matter in 2H-NbS<sub>2</sub>. *Phys. Rev. B*, 85:174517, 2012.
- [6] C. Bechinger, R. Di Leonardo, H. Löwen, C. Reichhardt, G. Volpe, and G. Volpe. Active particles in complex and crowded environments. *Rev. Mod. Phys.*, 88:045006, 2016.
- [7] A. Vanossi, N. Manini, M. Urbakh, S. Zapperi, and E. Tosatti. Colloquium: Modeling friction: From nanoscale to mesoscale. *Rev. Mod. Phys.*, 85:529–552, 2013.
- [8] J. M. Carlson and J. S. Langer. Properties of earthquakes generated by fault dynamics. *Phys. Rev. Lett.*, 62(22):2632–2635, 1989.
- [9] D. J. Pine, J. P. Gollub, J. F. Brady, and A. M. Leshansky. Chaos and threshold for irreversibility in sheared suspensions. *Nature (London)*, 438(7070):997–1000, 2005.
- [10] L. Corté, P. M. Chaikin, J. P. Gollub, and D. J. Pine. Random organization in periodically driven systems. *Nature Phys.*, 4(5):420–424, 2008.
- [11] C. F. Schreck, R. S. Hoy, M. D. Shattuck, and C. S. O’Hern. Particle-scale reversibility in athermal particulate media below jamming. *Phys. Rev. E*, 88(5):052205, 2013.
- [12] L. Milz and M. Schmiedeberg. Connecting the random organization transition and jamming within a unifying model system. *Phys. Rev. E*, 88(6):062308, 2013.
- [13] C. Zhou, C. J. Olson Reichhardt, C. Reichhardt, and I. Beyerlein. Random organization in periodically driven gliding dislocations. *Phys. Lett. A*, 378(22):1675–1678, 2014.
- [14] X. Ni, H. Zhang, D. B. Liarte, L. W. McFaul, K. A. Dahmen, J. P. Sethna, and J. R. Greer. Yield precursor dislocation avalanches in small crystals: The irreversibility transition. *Phys. Rev. Lett.*, 123(3):035501, 2019.
- [15] I. Regev, T. Lookman, and C. Reichhardt. Onset of irreversibility and chaos in amorphous solids under periodic shear. *Phys. Rev. E*, 88(6):062401, 2013.
- [16] I. Regev, J. Weber, C. Reichhardt, K. A. Dahmen, and T. Lookman. Reversibility and criticality in amorphous solids. *Nature Commun.*, 6(1):8805, 2015.
- [17] N. V. Priezjev. Reversible plastic events during oscillatory deformation of amorphous solids. *Phys. Rev. E*, 93(1):013001, 2016.
- [18] P. Leishangthem, A. D. S. Parmar, and S. Sastry. The yielding transition in amorphous solids under oscillatory shear deformation. *Nature Commun.*, 8(1):14653, 2017.
- [19] P. K. Jana, M. J. Alava, and S. Zapperi. Irreversibility transition of colloidal polycrystals under cyclic deformation. *Sci. Rep.*, 7(1):45550, 2017.
- [20] N. Mangan, C. Reichhardt, and C. J. Olson Reichhardt. Reversible to irreversible flow transition in periodically driven vortices. *Phys. Rev. Lett.*, 100(18):187002, 2008.
- [21] S. Okuma, Y. Tsugawa, and A. Motohashi. Transition from reversible to irreversible flow: Absorbing and depinning transitions in a sheared-vortex system. *Phys. Rev. B*, 83(1):012503, 2011.
- [22] M. Dobroka, Y. Kawamura, K. Ienaga, S. Kaneko, and S. Okuma. Memory formation and evolution of the vortex configuration associated with random organization. *New J. Phys.*, 19(5):053023, 2017.
- [23] B. L. Brown, C. Reichhardt, and C. J. O. Reichhardt. Reversible to irreversible transitions in periodically driven skyrmion systems. *New J. Phys.*, 21(1):013001, 2019.

- [24] C. Reichhardt, Ido Regev, K. Dahmen, S. Okuma, and C. J. O. Reichhardt. Reversible to irreversible transitions in periodic driven many-body systems and future directions for classical and quantum systems. *Phys. Rev. Res.*, 5:021001, 2023.
- [25] K. Harada, O. Kamimura, H. Kasai, T. Matsuda, A. Tonomura, and V. V. Moshchalkov. Direct observation of vortex dynamics in superconducting films with regular arrays of defects. *Science*, 274(5290):1167–1170, 1996.
- [26] C. Reichhardt, C. J. Olson, and F. Nori. Commensurate and incommensurate vortex states in superconductors with periodic pinning arrays. *Phys. Rev. B*, 57:7937–7943, 1998.
- [27] T. Bohlein, J. Mikhael, and C. Bechinger. Observation of kinks and antikinks in colloidal monolayers driven across ordered surfaces. *Nature Mater.*, 11(2):126–130, 2012.
- [28] N. Nagaosa and Y. Tokura. Topological properties and dynamics of magnetic skyrmions. *Nature Nanotechnol.*, 8(12):899–911, December 2013.
- [29] S.-G. Je, H.-S. Han, S. K. Kim, S. A. Montoya, W. Chao, I.-S. Hong, E. E. Fullerton, K.-S. Lee, K.-J. Lee, M.-Y. Im, and J.-I. Hong. Direct demonstration of topological stability of magnetic skyrmions *via* topology manipulation. *ACS Nano*, 14(3):3251–3258, March 2020.
- [30] C. J. Olson Reichhardt, S. Z. Lin, D. Ray, and C. Reichhardt. Comparing the dynamics of skyrmions and superconducting vortices. *Physica C*, 503:52–57, 2014.
- [31] C. Reichhardt, C. J. O. Reichhardt, and M. Milošević. Statics and dynamics of skyrmions interacting with disorder and nanostructures. *Rev. Mod. Phys.*, 94:035005, 2022.
- [32] K. Litzius, I. Lemesh, B. Krüger, P. Bassirian, L. Caretta, K. Richter, F. Büttner, K. Sato, O. A. Tretiakov, J. Förster, R. M. Reeve, M. Weigand, I. Bykova, H. Stoll, G. Schütz, G. S. D. Beach, and M. Kläui. Skyrmion Hall effect revealed by direct time-resolved X-ray microscopy. *Nature Phys.*, 13(2):170–175, 2017.
- [33] J. Iwasaki, M. Mochizuki, and N. Nagaosa. Universal current-velocity relation of skyrmion motion in chiral magnets. *Nature Commun.*, 4(1):1463, February 2013.
- [34] W. Jiang, X. Zhang, G. Yu, W. Zhang, X. Wang, M. B. Jungfleisch, J. E. Pearson, X. Cheng, O. Heinonen, K. L. Wang, Y. Zhou, A. Hoffmann, and S. G. E. te Velthuis. Direct observation of the skyrmion Hall effect. *Nature Phys.*, 13(2):162–169, 2017.
- [35] S.-Z. Lin, C. Reichhardt, C. D. Batista, and A. Saxena. Driven skyrmions and dynamical transitions in chiral magnets. *Phys. Rev. Lett.*, 110(20):207202, May 2013.
- [36] S.-Z. Lin, C. Reichhardt, C. D. Batista, and A. Saxena. Particle model for skyrmions in metallic chiral magnets: Dynamics, pinning, and creep. *Phys. Rev. B*, 87(21):214419, June 2013.
- [37] J. Feilhauer, S. Saha, J. Tobik, M. Zelent, L. J. Heyderman, and M. Mruczkiewicz. Controlled motion of skyrmions in a magnetic antidot lattice. *Phys. Rev. B*, 102(18):184425, November 2020.
- [38] C. Reichhardt, D. Ray, and C. J. Olson Reichhardt. Quantized transport for a skyrmion moving on a two-dimensional periodic substrate. *Phys. Rev. B*, 91(10):104426, March 2015.
- [39] C. Reichhardt, D. Ray, and C. J. O. Reichhardt. Nonequilibrium phases and segregation for skyrmions on periodic pinning arrays. *Phys. Rev. B*, 98(13):134418, October 2018.
- [40] N. P. Vizirim, J. C. Bellizotti Souza, C. Reichhardt, C. J. O. Reichhardt, and P. A. Venegas. Directional locking and the influence of obstacle density on skyrmion dynamics in triangular and honeycomb arrays. *J. Phys: Condens. Matter*, 33(30):305801, June 2021.
- [41] N. P. Vizirim, C. Reichhardt, C. J. O. Reichhardt, and P. A. Venegas. Skyrmion dynamics and topological sorting on periodic obstacle arrays. *New J. Phys.*, 22(5):53025, May 2020.
- [42] C. Reichhardt and C. J. O. Reichhardt. Commensuration effects on skyrmion Hall angle and drag for manipulation of skyrmions on two-dimensional periodic substrates. *Phys. Rev. B*, 105(21):214437, 2022.
- [43] N. P. Vizirim, C. Reichhardt, P. A. Venegas, and C. J. O. Reichhardt. Guided skyrmion motion along pinning array interfaces. *J. Mag. Mag. Mater.*, 528:167710, June 2021.
- [44] C.-L. Zhang, J.-N. Wang, C.-K. Song, N. Mehmood, Z.-Z. Zeng, Y.-X. Ma, J.-B. Wang, and Q.-F. Liu. Edge-guided heart-shaped skyrmion. *Rare Metals*, 41(3):865–870, March 2022.
- [45] C. Reichhardt, D. Ray, and C. J. Olson Reichhardt. Magnus-induced ratchet effects for skyrmions interacting with asymmetric substrates. *New J. Phys.*, 17(7):73034, July 2015.
- [46] J. C. Bellizotti Souza, N. P. Vizirim, C. J. O. Reichhardt, C. Reichhardt, and P. A. Venegas. Skyrmion ratchet in funnel geometries. *Phys. Rev. B*, 104(5):54434, August 2021.
- [47] W. Chen, L. Liu, Y. Ji, and Y. Zheng. Skyrmion ratchet effect driven by a biharmonic force. *Phys. Rev. B*, 99(6):64431, February 2019.
- [48] B. Göbel and I. Mertig. Skyrmion ratchet propagation: utilizing the skyrmion Hall effect in AC racetrack storage devices. *Sci. Rep.*, 11(1):3020, February 2021.
- [49] J. C. Bellizotti Souza, N. P. Vizirim, C. J. O. Reichhardt, C. Reichhardt, and P. A. Venegas. Controlled skyrmion ratchet in linear protrusion defects. *Phys. Rev. B*, 109(5):054407, 2024.

- [50] R. Yanes, F. Garcia-Sanchez, R. F. Luis, E. Martinez, V. Raposo, L. Torres, and L. Lopez-Diaz. Skyrmion motion induced by voltage-controlled in-plane strain gradients. *Appl. Phys. Lett.*, 115(13):132401, September 2019.
- [51] S. L. Zhang, W. W. Wang, D. M. Burn, H. Peng, H. Berger, A. Bauer, C. Pfleiderer, G. van der Laan, and T. Hesjedal. Manipulation of skyrmion motion by magnetic field gradients. *Nature Commun.*, 9(1):2115, May 2018.
- [52] K. Everschor, M. Garst, B. Binz, F. Jonietz, S. Mühlbauer, C. Pfleiderer, and A. Rosch. Rotating skyrmion lattices by spin torques and field or temperature gradients. *Phys. Rev. B*, 86(5):54432, August 2012.
- [53] L. Kong and J. Zang. Dynamics of an insulating skyrmion under a temperature gradient. *Phys. Rev. Lett.*, 111(6):67203, August 2013.
- [54] X. Gong, H. Y. Yuan, and X. R. Wang. Current-driven skyrmion motion in granular films. *Phys. Rev. B*, 101(6):064421, February 2020.
- [55] N. Del-Valle, J. Castell-Queralt, L. González-Gómez, and C. Navau. Defect modeling in skyrmionic ferromagnetic systems. *APL Mater.*, 10:10702, 2022.
- [56] H. Y. Yuan, X. S. Wang, Man-Hong Yung, and X. R. Wang. Wiggling skyrmion propagation under parametric pumping. *Phys. Rev. B*, 99(1):014428, January 2019.
- [57] X. Zhang, Y. Zhou, M. Ezawa, G. P. Zhao, and W. Zhao. Magnetic skyrmion transistor: skyrmion motion in a voltage-gated nanotrack. *Sci. Rep.*, 5(1):11369, June 2015.
- [58] L. Zhao, X. Liang, J. Xia, G. Zhao, and Y. Zhou. A ferromagnetic skyrmion-based diode with a voltage-controlled potential barrier. *Nanoscale*, 17:9507, 2020.
- [59] X. Zhang, J. Xia, and X. Liu. Structural transition of skyrmion quasiparticles under compression. *Phys. Rev. B*, 105(18):184402, 2022.
- [60] J. C. Bellizotti Souza, N. P. Vizarim, C. J. O. Reichhardt, C. Reichhardt, and P. A. Venegas. Spontaneous skyrmion conformal lattice and transverse motion during dc and ac compression. *New J. Phys.*, 25(5):053020, May 2023.
- [61] N. P. Vizarim, J. C. Bellizotti Souza, C. J. O. Reichhardt, C. Reichhardt, M. V. Milošević, and P. A. Venegas. Soliton motion in skyrmion chains: Stabilization and guidance by nanoengineered pinning. *Phys. Rev. B*, 105(22):224409, 2022.
- [62] J. C. Bellizotti Souza, N. P. Vizarim, C. J. O. Reichhardt, C. Reichhardt, and P. A. Venegas. Soliton motion induced along ferromagnetic skyrmion chains in chiral thin nanotracks. *J. Mag. Mag. Mater.*, 587:171280, 2023.
- [63] D. Song, W. Wang, S. Zhang, Y. Liu, N. Wang, F. Zheng, M. Tian, R. E. Dunin-Borkowski, J. Zang, and H. Du. Steady motion of 80-nm-size skyrmions in a 100-nm-wide track. *Nature Commun.*, 15:5614, 2024.
- [64] C. Liu, J. Wang, W. He, C. Zhang, S. Zhang, S. Yuan, Z. Hou, M. Qin, Y. Xu, X. Gao, Y. Peng, K. Liu, Z. Q. Qiu, J.-M. Liu, and X. Zhang. Strain-induced reversible motion of skyrmions at room temperature. *ACS Nano*, 18(1):761–769, 2024.
- [65] X. Xing and Y. Zhou. Skyrmion motion and partitioning of domain wall velocity driven by repulsive interactions. *Commun. Phys.*, 5(1):1–11, 2022.
- [66] J. C. Bellizotti Souza, N. P. Vizarim, C. J. O. Reichhardt, P. A. Venegas, and C. Reichhardt. Skyrmion Molecular Crystals and Superlattices on Triangular Substrates, 2024. arXiv:2407.20188 [cond-mat].
- [67] G. R. Berdiyrov, M. V. Milošević, and F. M. Peeters. Vortex configurations and critical parameters in superconducting thin films containing antidot arrays: Nonlinear Ginzburg-Landau theory. *Phys. Rev. B*, 74:174512, 2006.
- [68] J. S. Neal, M. V. Milošević, S. J. Bending, A. Potenza, L. San Emeterio, and C. H. Marrows. Competing symmetries and broken bonds in superconducting vortex-antivortex molecular crystals. *Phys. Rev. Lett.*, 99:127001, 2007.
- [69] C. Reichhardt and C. J. Olson Reichhardt. Vortex molecular crystal and vortex plastic crystal states in honeycomb and kagomé pinning arrays. *Phys. Rev. B*, 76(6):064523, 2007.
- [70] C. Reichhardt and C. J. Olson. Novel colloidal crystalline states on two-dimensional periodic substrates. *Phys. Rev. Lett.*, 88(24):248301, 2002.
- [71] M. Brunner and C. Bechinger. Phase behavior of colloidal molecular crystals on triangular light lattices. *Phys. Rev. Lett.*, 88(24):248302, May 2002. Publisher: American Physical Society.
- [72] R. Agra, F. van Wijland, and E. Trizac. Theory of orientational ordering in colloidal molecular crystals. *Phys. Rev. Lett.*, 93(1):018304, 2004.
- [73] A. Šarlah, T. Franosch, and E. Frey. Melting of colloidal molecular crystals on triangular lattices. *Phys. Rev. Lett.*, 95:088302, 2005.
- [74] A. Šarlah, E. Frey, and T. Franosch. Spin models for orientational ordering of colloidal molecular crystals. *Phys. Rev. E*, 75:021402, 2007.

- [75] A. P. Reddy, T. Devakul, and L. Fu. Artificial atoms, Wigner molecules, and an emergent kagome lattice in semiconductor moiré superlattices. *Phys. Rev. Lett.*, 131(24):246501, 2023.
- [76] H. Li, Z. Xiang, A. P. Reddy, T. Devakul, R. Sailus, R. Banerjee, T. Taniguchi, K. Watanabe, S. Tongay, A. Zettl, L. Fu, M. F. Crommie, and F. Wang. Wigner molecular crystals from multielectron moiré artificial atoms. *Science*, 385(6704):86–91, 2024.
- [77] R. F. L. Evans. Atomistic Spin Dynamics. In W. Andreoni and S. Yip, editors, *Handbook of Materials Modeling: Applications: Current and Emerging Materials*, pages 1–23. Springer International Publishing, 2018.
- [78] J. Iwasaki, M. Mochizuki, and N. Nagaosa. Current-induced skyrmion dynamics in constricted geometries. *Nature Nanotechnol.*, 8(10):742–747, October 2013.
- [79] S. Paul, S. Haldar, S. von Malottki, and S. Heinze. Role of higher-order exchange interactions for skyrmion stability. *Nature Commun.*, 11(1):4756, 2020.
- [80] S. Seki and M. Mochizuki. *Skyrmions in Magnetic Materials*. Springer International Publishing, 2016.
- [81] T. L. Gilbert. A phenomenological theory of damping in ferromagnetic materials. *IEEE Trans. Mag.*, 40(6):3443–3449, 2004.
- [82] J. Zang, M. Mostovoy, J. H. Han, and N. Nagaosa. Dynamics of Skyrmion Crystals in Metallic Thin Films. *Phys. Rev. Lett.*, 107(13):136804, September 2011.
- [83] See Supplemental Material for supplementary videos.